NANO LETTERS
Cite This: Nano Lett. 2018, 18, 6144−6149
Letter
pubs.acs.org/NanoLett

Helical Hole State in Multiple Conduction Modes in Ge/Si Core/Shell Nanowire

Jian Sun,[*,†,‡] Russell S. Deacon,[†,§] Rui Wang,[†] Jun Yao,[∥,⊥] Charles M. Lieber,[∥,#] and Koji Ishibashi[†,§]

[†]Advanced Device Laboratory, RIKEN, 2-1 Hirosawa,Wako, Saitama 351-0198, Japan
[‡]School of Physical Science and Electronics, Central South University, Changsha 410083, China
[§]Center for Emergent Matter Science, RIKEN, Wako, Saitama 351-0198, Japan
[∥]Deparment of Chemistry and Chemical Biology, Harvard University, Cambridge, Massachusetts 02138, United States
[⊥]Department of Electrical and Computer Engineering, Institute for Applied Life Sciences, University of Massachusetts, Amherst, Massachusetts 01003, United States
[#]School of Engineering and Applied Sciences, Harvard University, Cambridge, Massachusetts 02138, United States

Supporting Information

ABSTRACT: Helical states, a prerequisite for the engineering of Majorana zero modes in solid-state systems, have recently been reported in the conduction band of III−V nanowires (NWs) subject to strong Rashba spin−orbit interaction. We report the observation of re-entrant conductance features consistent with the presence of helical hole states in multiple conduction modes of a Ge/Si core/shell NW. The Ge/Si system has several potential advantages over electron systems such as longer spin coherence time due to weaker coupling to nuclear spins and the possibility of isotope-purified materials for nuclear spin-free devices. We derive the Landé g factor of 3.6 from magneto-transport measurements, comparable to theoretical predictions and significantly larger when compared with that in strongly confined quantum dots. The spin−orbit energy is evaluated as ∼2.1 meV, on par with values in III−V NWs, showing good agreement with previous theoretical predictions and weak antilocalization measurements.

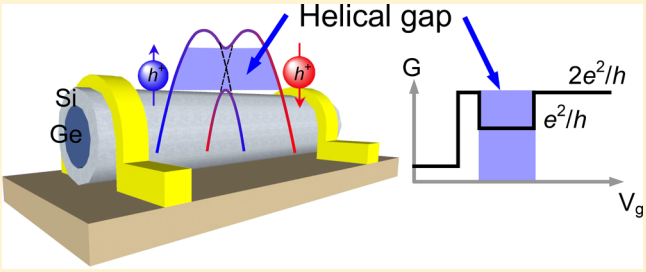

KEYWORDS: *Ge/Si nanowire, quantum point contact, hole helical state, spin−orbit interaction*

A helical state, exhibiting spin momentum locking, is predicted to emerge in 1D ballistic semiconductor nanowires (NWs) possessing strong Rashba spin−orbit interaction under certain conditions. Such a helical state is a key ingredient for the realization of Majorana zero modes[1,2] and has applications for spin filtering[3] and Cooper pair splitters.[4] A distinct experimental signature of the helical state is a re-entrant conductance gap feature at the $2e^2/h$ conductance plateau measured in a quantum point contact (QPC) device as different portions of the band dispersion are probed. To observe this signature in experiments is, however, challenging; numerical studies point out that some key geometrical and physical device parameters must be met simultaneously to resolve the helical state gap and distinguish it from Fabry−Pérot interference and effects of disorder.[5] Recently the helical state has been experimentally detected in the lowest subband of InAs[6] and InSb[7] NWs. In addition, helical gap features have been detected in 1D channels defined in a GaAs quantum hole-gas.[8] Hole systems offer several potential advantages for spintronics and quantum information processing applications; having an effective spin of $J = 3/2$, momentum and spin can be strongly coupled to allow electric-field-mediated spin manipulation. Additionally, hole-spin lifetimes can be prolonged in the presence of confinement.[9,10] However, the hole-spin regime is difficult to reach in conventional III−V NWs with only a few experimental studies of the spin properties.[11]

Germanium/silicon core/shell NWs are a promising system for the study of 1D hole states. Owing to a large valence band offset of ∼0.5 eV between Ge and Si, holes are naturally accumulated in the Ge core and strongly confined by the interface with the Si shell.[12,13] The dopant-free growth leads to the high mobility with mean-free-path up to ∼500 nm.[13] In addition, both Ge and Si have a low density of nuclear spins (or can be grown with zero net nuclear spin), which, through hyperfine coupling, are the typical leading contributor to the limit of spin coherence times for III−V-based qubit devices.[14−16] More importantly, a strong dipole-coupled Rashba-type spin−orbit interaction (SOI) is predicted in

Received: May 3, 2018
Revised: September 14, 2018
Published: September 18, 2018

DOI: 10.1021/acs.nanolett.8b01799
Nano Lett. 2018, 18, 6144−6149

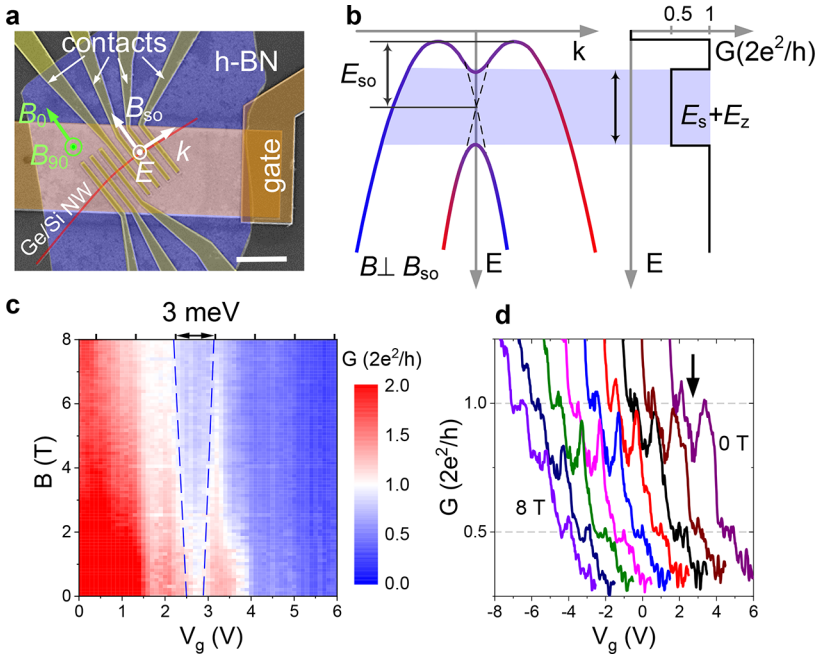

Figure 1. (a) False color scanning electron micrograph of the device. A Ge/Si NW (red) with Ti/Pd contacts (yellow) is located on a gold bottom gate (orange) with h-BN (blue) as the dielectric layer. Rashba spin−orbit field B_{so} is perpendicular to **k** and **E**. The scale bar is 2 μm. (b) Energy dispersion of two spin sub-bands with SOI and a B field perpendicular to B_{so}. The helical gap is opened by the Zeeman energy, E_z, in addition to a zero-field gap, E_s, possibly opened by two-particle backscattering, leading to a re-entrant conductance from integer to half-integer $2e^2/h$. (c) Quantized conductance of the first mode as a function of $B \perp B_{so}$ (first cool down). The linear expansion of the re-entrant conductance is marked with blue dashed lines. The upper energy scale bar indicates the relative energy change calculated from the gate voltage using a lever arm of ~3.3 meV/V. (d) Line traces cut from the 2D map in panel c from 0 to 8 T with 1 T steps. The black arrow indicates the conductance drop corresponding to the re-entrant conductance feature. The line traces are shifted horizontally for clarity.

Ge/Si NWs as a result of the quasi-degeneracy in its low-energy valence bands;[17] as such, Ge/Si core/shell NWs are a promising material system to investigate helical hole states. However, considering its relatively low Landé g factor, to detect the helical gap in Ge/Si NW is technically challenging.

Here we report the evidence of helical hole states in a QPC formed in a Ge/Si core/shell NW. The helical hole state is detected as a re-entrant conductance feature on conductance plateaus observed at integer multiples of $2e^2/h$. Surprisingly, we find re-entrant conductance features consistent with the helical state in multiple conduction modes. The attribution of this feature to a helical spin-gap is supported by both magnetic field dependence and angular dependence, from which we also extract a strong spin−orbit energy E_{so} = 2.1 meV and large Landé g factor of 3.6.

Figure 1a shows a schematic of a typical device. A Ge/Si NW of ~15 nm in diameter (Ge core diameter ~9 nm and Si shell thickness ~3 nm) is placed on a gold bottom gate covered with a ~30 nm thick h-BN flake used as a dielectric layer. The QPC is formed in the NW between any two Ti/Pd contacts, which are fabricated with separations ranging from 240 to 330 nm. The relatively thick h-BN dielectric helps to ensure an adiabatic potential profile in the NW, which is a key factor to observe the helical gap in a 1D system superimposed with Fabry−Pérot inference.[5] In the following, we present the results measured in one QPC with a length of 280 nm. Data from an additional NW are provided in the Supporting Information. All measurements are performed at a temperature of 7.5 K to suppress conductance fluctuations that otherwise mask the re-entrant conductance features being discussed. This specific temperature is chosen by raising the temperature from the base temperature of 1.4 K until the conductance fluctuations are suppressed and relatively clear quantized conductance plateaus and re-entrant conductance features appear (see the Supporting Information).

The subband occupation of the QPC can be set by controlling the chemical potential using bottom gate voltage, V_g. The presence of the substrate and gate imposes an out-of-plane electric field, **E**, resulting in an in-plane Rashba spin−orbit field, $B_{so} \propto \mathbf{k} \times \mathbf{E}$, ideally oriented normal to the wire, where **k** is momentum. As shown in Figure 1b, this SOI laterally shifts the two spin-degenerate subbands in momentum space and lifts the degeneracy. However, Kramers degeneracy is still preserved, which holds the conductance at an integral multiple of $2e^2/h$. Applying a magnetic field B perpendicular to B_{so} can open a helical gap of $E_z = g\mu_B B$, with g and μ_B being the Landé g factor and Bohr magneton, respectively. It is also known that through exchange interactions it is possible to hybridize two spin subbands and open a gap-like feature in the absence of an external magnetic field,[6] as illustrated in Figure 1b. Overall, the helical gap can be probed in measurements as a re-entrant conductance feature from integer to half-integer $2e^2/h$.

Figure 1c shows differential conductance, G, measured in the vicinity of the first mode as a function of gate voltage, V_g, and magnetic field, B, applied perpendicular to the substrate surface. Line traces cut at a range of B fields are shown in Figure 1d. Quantized conductance plateaus at e^2/h and $2e^2/h$ are observed at all B fields, revealing a QPC possibly possessing both spin−orbit interaction and strong electron−electron interaction.[18−20] In the Ge/Si NW with a core diameter of 9 nm, the hole subband separation is only a few millielectronvolts.[21] On the $2e^2/h$ plateau, a pronounced conductance dip is observed, as indicated by the black arrow in Figure 1d.

DOI: 10.1021/acs.nanolett.8b01799
Nano Lett. 2018, 18, 6144−6149

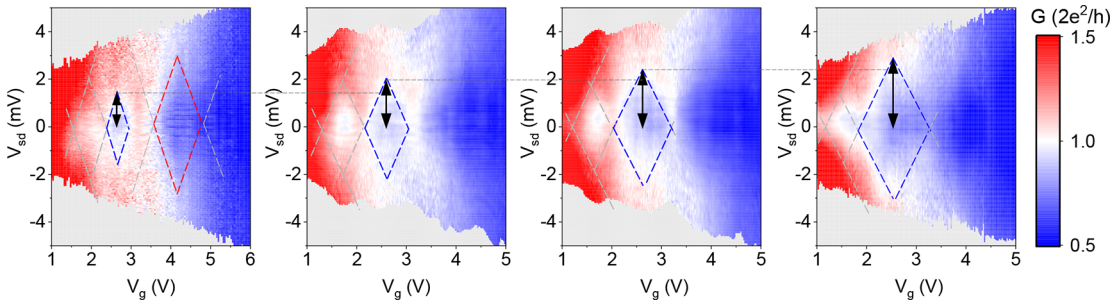

Figure 2. Differential conductance, G, measured as a function of V_g and V_{sd} in perpendicular fields, B, of 0, 2, 4.5, and 8 T (from left to right, first cool down). Dashed diamonds are a guide to the eye, indicating the conductance plateaus. The blue dashed lines indicate the perimeter of the helical gap region. The red dashed lines indicate the perimeter of the e^2/h plateau at zero field. Black arrows indicate the helical gap energy spacing. The horizontal dashes are provided to help to identify the development of helical gap.

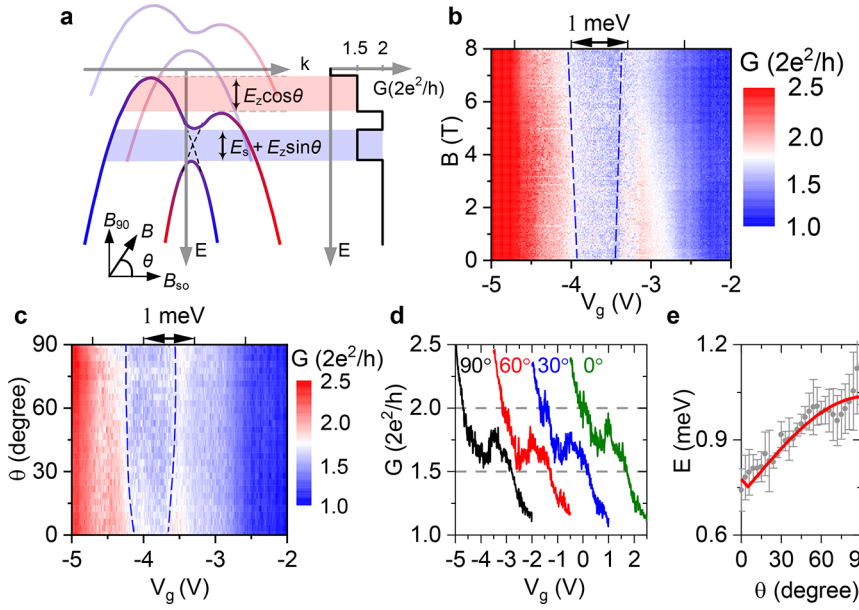

Figure 3. (a) Energy dispersion of the second subband with SOI at a B field tilted by an angle θ to B_{so}. The helical gap size is given by $E_s + E_z \cdot \sin\theta$. The two subbands are Zeeman split by an additional energy of $E_z \cdot \cos\theta$, resulting in the half-integer $2e^2/h$ conductance. Note, as a simplified schematic, the more complex picture, for example, avoided level crossing due to the hybridization of subbands, is not presented. (b) Quantized conductance in the second mode as a function of perpendicular B field (second cool down). Blue dashed lines highlight the linear expansion of the re-entrant conductance feature. The upper energy scale bar indicates the relative energy change calculated with a lever arm of ~1.4 meV/V. (c) Quantized conductance at B = 6 T as a function of tilt angle θ to B_{so}. The evolution of the re-entrant conductance feature is highlighted using the blue dashed lines. (d) Line traces cut from the 2D map in panel c at various angles. They are shifted horizontally for clarity. (e) Helical gap energy (gray dots) extracted from panel c. Red solid line is the fit using $E = E_s + E_z \cdot |\sin(\theta + \theta_0)|$.

Importantly, it expands linearly with increasing magnetic field, as expected for the re-entrant conductance feature corresponding to the helical gap. Some weak conductance oscillations are noticed. We identify them as Fabry–Pérot oscillations or other conductance fluctations, which can be distinguished from the re-entrant conductance feature because they possess negligible magnetic response appearing as vertical "strip" features in Figure 1c. We note that the re-entrant conductance remains at B = 0 T, indicating a zero-field gap of E_s. A similar phenomenon has been reported previously by Heedt et al. and Pedder et al.,[6,22] in which the feature was referred to as a "pseudo-gap" introduced by the emergence of correlated two-particle backscattering and Rashba SOI. However, the feature remains under debate and can be similar in appearance to the resonance-type conductance dip induced by two-particle electron scattering in a Rashba NW or even the presence of an impurity state lying just below the band.[23,24] Furthermore, the re-entrant conductance does not actually return to e^2/h, as may be expected if we consider a more realistic picture, with superimposed Fabry–Pérot oscillations, inevitable disorder, possible tunneling through the gap regime, and the relatively high temperature of the measurement.[5]

Quantized conductance plateaus and the re-entrant conductance can be observed in the voltage bias spectroscopy, as shown in Figure 2. Changing B field from 0 to 8 T enhances the energy of the helical gap from the zero-field gap of 1.51 to 3.14 meV as a result of the increasing E_z, indicating a g factor of ~3.5. A diamond corresponding to the e^2/h plateau is also observed at zero field, which is consistent with the data presented in Figure 1d. From Figure 2, we estimate the gate lever arm to be ~3.3 meV/V; therefore, a comparable g factor of ~3.6 and a zero-field gap $E_s \approx 1.5$ meV can also be evaluated from the magneto-transport measurements plotted in Figure 1c. Our evaluated g factor is larger than previously reported values of $g \approx 2$ found in strongly confined quantum dots[25−27]

DOI: 10.1021/acs.nanolett.8b01799
Nano Lett. 2018, 18, 6144−6149

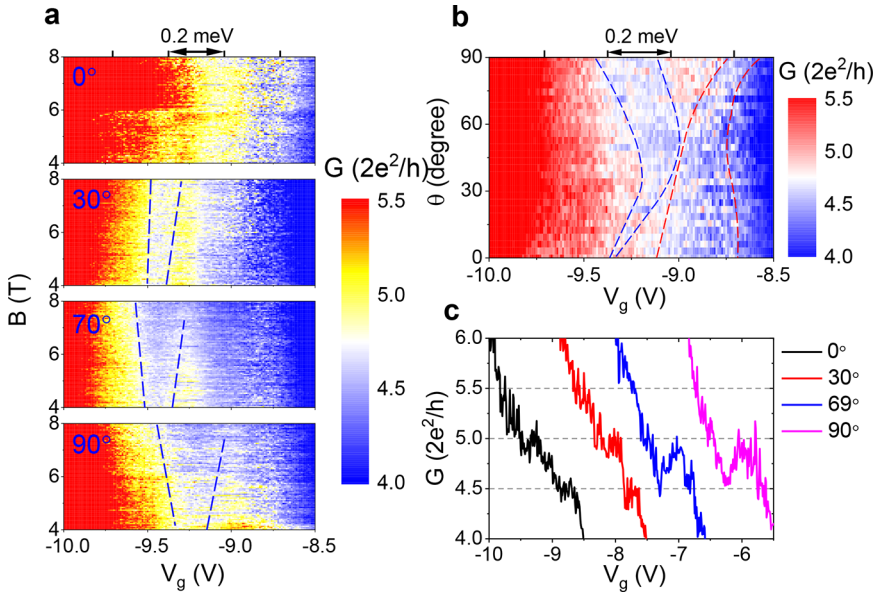

Figure 4. (a) B dependence of the quantized conductance in the fifth mode measured with B oriented at various angles θ (second cool down). The re-entrant conductance feature is marked with blue dashed lines. The upper energy scale bar indicates the relative energy change calculated using the lever arm of ~0.6 meV/V. (b) θ dependence of the fifth mode measured at B = 5 T. The evolution of the re-entrant conductance feature is indicated by the blue dashed lines. Red dashed lines highlight the shoulder of 4.5 × $2e^2/h$ caused by an additional Zeeman splitting of $E_z \cdot \cos\theta$. (c) Line traces cut from panel b. They are shifted horizontally for clarity.

but is in good agreement with the theoretical prediction for the Ge/Si NW in weak electric field of ~1 V/μm.[28]

The strength of the SOI E_{so} is roughly given by the energy difference between the bottom of the subband to the center of the helical gap at zero B field, as indicated in Figure 1b. We calculate its value as ~2.1 meV, corresponding to a spin−orbit length $l_{so} = \hbar/\sqrt{2E_{so}m^*} \approx 7.9$ nm with $m^* = 0.28m_0$. The effective mass of the heavy hole is used because it is predominant in the low-energy regime in the Ge/Si NW.[13] This result is consistent with an estimate of E_{so} = 1.5 to 3 meV, evaluated in our previous weak antilocalization measurements.[29] The Rashba coefficient is, therefore, calculated as $\alpha = \hbar\sqrt{2E_{so}/m^*} \approx 0.34$ eVÅ.

An important test of the helical gap opened can be performed by considering the angular B-field dependence. The Hamiltonian for the Rashba SOI is given as $\hat{H}_R = (\alpha/\hbar)(\mathbf{z} \times \mathbf{k})\cdot\sigma$, where $\mathbf{z}$ is a unit vector along electric field, $\mathbf{E}$, and σ is the vector of Pauli spin matrices.[30] Accordingly, rotating B to B_{so} (θ from 90 to 0°) closes the helical gap sinusoidally while keeping the zero-field gap, E_s, untouched (Figure 3a). Magnetic-field-induced opening of the helical gap is governed only by the B component perpendicular to B_{so} as $E_z \cdot \sin\theta$. When B is aligned with B_{so}, the spin mixing vanishes, and we expect a quenched helical gap. Additionally, when rotating B, two subbands are Zeeman split by an additional energy of $E_z \cdot \cos\theta$.[7] This angle dependency is a unique feature of the SOI and can be used to confirm its origin for the re-entrant conductance feature.

Nevertheless, in reality, the NW inevitably hosts charged impurities, resulting in local electric-field fluctuations comparable to the gate-induced $\mathbf{E}$, which could vary the orientation of B_{so} locally. In addition, to perform the angular dependence measurement, the fridge temperature is cycled and device is remounted. Unfortunately, after the thermal cycle, the measurement at the first subband is found to be unstable, with the observed gap size being inconsistent in repeated gates sweeps when in an applied magnetic field. This may be caused by the redistribution of charged impurities, resulting in the fluctuation of the orientation of B_{so} along the channel length. Some higher subbands, that is, second and fifth subbands, were, however, found to be stable, as the charged impurity is mostly screened, and so measurements are performed there.

To verify the consistency between the helical gap predicted by spin−orbit theory and the measured re-entrant conductance feature, we investigate its θ dependence in the second mode. Here the device is remounted on a single axis rotator, with which the sample substrate can be rotated in the magnetic field with the NW as the axis. Following this thermal cycle and remounting of the device, we reconfirm the presence of a helical gap in the second mode with B-dependence measurements, which reveals a linear expansion of the re-entrant conductance gap with B, as indicated in Figure 3b. Using a lever arm of ~1.4 meV/V, we evaluate E_z^{8T} = 0.39 meV, E_s = 0.74 meV, and g = 0.9. Note that the enhanced carrier density of the NW in the second mode results in a lower gate lever-arm compared with that in the first mode. Interestingly, this helical gap is quite robust, as it is reproducible after a temperature cycle from low to ambient temperature. Figure 3c,d indicated the θ dependence of quantized conductance at B of 6 T rotating from θ = 90 to 0°. As the external B field is rotated into the sample plane, the helical gap is decreased. We plot the helical gap energy as a function of θ in Figure 3e. It can be fitted well using the sinusoidal equation $E_s + E_z \cdot |\sin(\theta + \theta_0)|$, where θ_0 denotes a nominal misalignment of B_{so}. The fitting indicates E_z^{6T} = 0.29 meV, E_s = 0.76 meV, g = 0.9, and θ_0 = 6.4°, which are consistent with parameters determined from the B dependence in Figure 3b. Combining the results of both B and θ dependence, we are convinced by the helical nature of the measured re-entrant conductance feature. The nonzero θ_0 implies that B_{so} slightly deviates from its ideal orientation (in-plane and normal to the NW axis), which can be ascribed to

DOI: 10.1021/acs.nanolett.8b01799
Nano Lett. 2018, 18, 6144−6149

the geometric misalignment in sample mounting and a possible strong localized electric field due to defects. Considering this misalignment and the existence of the zero-field gap, the helical gap always persists and is never fully quenched.

We now consider the device parameters, which facilitate the clear visibility of the helical gap in our experiment. The re-entrant conductance feature associated with the helical gap can be strongly masked by the superimposed Fabry–Pérot resonances, and the helical gap may easily remain indistinguishable in a realistic measurement. For instance, the Fabry–Pérot oscillations can be observed on plateaus in Figure 1d. To observe the helical gap feature, the gate potential profile in the NW must be adiabatic, as discussed by Rainis and Loss.[5] The optimal onset potential length, λ, is identified by the critical Zeeman length, $\lambda^* = 2\hbar v_F/(E_z + E_s)$, with $v_F = \alpha/\hbar$ being the Fermi velocity at zero field. Then, we could calculate λ^* ranging from 22 to 45 nm using these parameters extracted from the first mode, while the actual onset length λ is estimated as ∼33 nm using finite-element simulations (Supporting Information). We find our extracted and simulated parameters are sufficiently close to ensure a good visibility of the helical gap in our measured QPC.

Finally, we present measurements carried out for the fifth conduction mode, which are consistent with the phenomena observed in the lower modes. Figure 4a presents B dependence, with B fixed at varied orientations. Figure 4b,c displays the θ dependence with B of 5 T and traces extracted from cuts at different θ, respectively. In both panels, the well-defined re-entrant conductance feature is observed and evolves as anticipated with B and θ. At high-index modes, electron–electron interaction strength is comparatively weaker due to the larger hole density, leading to a vanishing zero-field gap E_s. Thus the helical gap can be barely seen at $\theta = 0°$. g factor is found to be 0.6 from both B dependence and θ dependence, respectively. We observe a reduced g factor in higher conduction modes. This is possibly attributed to a larger effective mass in the higher modes or the enhanced electric field, which is predicted to tune the g factor in Ge/Si NWs.[28]

By investigating the re-entrant conductance feature emerging at quantized conductance plateaus, we detect the signature of a helical gap for multiple conduction modes in a Ge/Si NW QPC. A Landé g factor of 3.6 and spin–orbit energy of 2.1 meV are extracted for the first conduction mode, showing good agreement with previous theoretical predictions.[17,28] In view of such a strong spin–orbit interaction, together with the absence of nuclear spin, we envisage Ge/Si core/shell NWs as a promising material platform for the study of Majorana physics.

Experimental Section. Device Fabrication. The Ge/Si core/shell NW used in this work is epitaxially synthesized by a two-step vapor–liquid–solid method that has been described elsewhere.[31] First, a commercial available h-BN flake (Momentive, Polarthem grade PT110[32]) of ∼30 nm thickness was dry-transferred onto a predefined gold gate on a SiO_2/Si substrate using a homemade mechanical manipulator with a viscoelastic membrane (Gelfilm, Gelpak).[33] Then, the NW was transferred onto the h-BN using a PMMA stamping technique described in detail elsewhere.[34] Finally, electrical contacts were defined from Ti/Pd (0.5 nm/80 nm) using e-beam lithograph and evaporation. Before evaporation, a short dip in buffered hydrofluoric acid was carried out to strip the surface oxide of the NW.

Electrical Measurements. Measurements were performed in a pumped He-4 refrigerator at 7.5 K. This relatively high temperature ensures that the impact of Fabry–Pérot interference is lowered (see the Supporting Information). Two different sample inserts are used in this work. An insert with fixed external B field aligned perpendicular to the substrate surface was utilized for the measurements presented in Figures 1 and 2 (first cool down). Data presented in Figures 3 and 4 were obtained with a second sample insert (second cool down), on which the substrate can be manually rotated in the range 0–90° from perpendicular to parallel to the external B field. The NW was aligned by eye to the rotation axis with an accuracy within 10°. The device experienced a temperature cycle when we switched the insets, leading to some changes in the transport features, most notably a change in gate voltages at which plateaus and pinch-off were observed. The differential conductance, G, was measured using standard lock-in techniques with an excitation voltage of <100 μV and a frequency f = 74.7 Hz. In all data presented in this Communication, a background resistance, arising from contact and lead regions, has been subtracted. This background resistance is determined by aligning conductance plateaus to multiples of $2e^2/h$ (see the Supporting Information).

■ ASSOCIATED CONTENT

Supporting Information

The Supporting Information is available free of charge on the ACS Publications website at DOI: 10.1021/acs.nanolett.8b01799.

Quantized conductance traces, temperature dependence of the quantized conductance measurements, simulation of the effective QPC length, additional measurements of bias spectroscopy, and measurements of a second device (PDF)

■ AUTHOR INFORMATION

Corresponding Author

*E-mail: jian.sun@riken.jp. Fax: +81-48-462-4659.

ORCID

Jian Sun: 0000-0002-7992-8092

Jun Yao: 0000-0002-5269-3190

Charles M. Lieber: 0000-0002-6660-2456

Notes

The authors declare no competing financial interest.

■ ACKNOWLEDGMENTS

We thank Stefan Ludwig for useful discussion and Hiroshi Mizuta for his support on COMSOL. This work was supported by RIKEN SPDR Fellowship, Grant-in-Aid for Young Scientists (No. 17K14076), Grant-in-Aid for Scientific Research (Nos. 16H02204 and 15H02015), and Grants-in-Aid for Scientific Research on Innovative Areas "Science of hybrid quantum systems" (No. 15H05867) from Japan Society for the Promotion of Science.

■ REFERENCES

(1) Lutchyn, R. M.; Sau, J. D.; Das Sarma, S. *Phys. Rev. Lett.* **2010**, *105* (7), 77001.

(2) Oreg, Y.; Refael, G.; von Oppen, F. *Phys. Rev. Lett.* **2010**, *105* (17), 177002.

(3) Sato, K.; Loss, D.; Tserkovnyak, Y. *Phys. Rev. Lett.* **2010**, *105* (22), 226401.

(4) Shekhter, R. I.; Entin-Wohlman, O.; Jonson, M.; Aharony, A. *Phys. Rev. Lett.* **2016**, *116* (21), 217001.

DOI: 10.1021/acs.nanolett.8b01799
Nano Lett. 2018, 18, 6144–6149

(5) Rainis, D.; Loss, D. *Phys. Rev. B: Condens. Matter Mater. Phys.* **2014**, *90* (23), 235415.
(6) Heedt, S.; Traverso Ziani, N.; Crépin, F.; Prost, W.; Trellenkamp, S.; Schubert, J.; Grützmacher, D.; Trauzettel, B.; SchäPers, T. *Nat. Phys.* **2017**, *13* (6), 563.
(7) Kammhuber, J.; Cassidy, M. C.; Pei, F.; Nowak, M. P.; Vuik, A.; Gül, Ö.; Car, D.; Plissard, S. R.; Bakkers, E. P. a. M.; Wimmer, M.; Kouwenhoven, L. P. *Nat. Commun.* **2017**, *8* (1), 478.
(8) Quay, C. H. L.; Hughes, T. L.; Sulpizio, J. A.; Pfeiffer, L. N.; Baldwin, K. W.; West, K. W.; Goldhaber-Gordon, D.; de Picciotto, R. *Nat. Phys.* **2010**, *6* (5), 336.
(9) Fischer, J.; Loss, D. *Phys. Rev. Lett.* **2010**, *105* (26), 266603.
(10) Brunner, D.; Gerardot, B. D.; Dalgarno, P. A.; Wüst, G.; Karrai, K.; Stoltz, N. G.; Petroff, P. M.; Warburton, R. J. *Science* **2009**, *325* (5936), 70−72.
(11) Pribiag, V. S.; Nadj-Perge, S.; Frolov, S. M.; van den Berg, J. W. G.; van Weperen, I.; Plissard, S. R.; Bakkers, E. P. a. M.; Kouwenhoven, L. P. *Nat. Nanotechnol.* **2013**, *8* (3), 170−174.
(12) Xiang, J.; Lu, W.; Hu, Y.; Wu, Y.; Yan, H.; Lieber, C. M. *Nature* **2006**, *441* (7092), 489.
(13) Lu, W.; Xiang, J.; Timko, B. P.; Wu, Y.; Lieber, C. M. *Proc. Natl. Acad. Sci. U. S. A.* **2005**, *102* (29), 10046−10051.
(14) Nowack, K. C.; Koppens, F. H. L.; Nazarov, Y. V.; Vandersypen, L. M. K. *Science* **2007**, *318* (5855), 1430−1433.
(15) Petersson, K. D.; McFaul, L. W.; Schroer, M. D.; Jung, M.; Taylor, J. M.; Houck, A. A.; Petta, J. R. *Nature* **2012**, *490* (7420), 380−383.
(16) van den Berg, J. W. G.; Nadj-Perge, S.; Pribiag, V. S.; Plissard, S. R.; Bakkers, E. P. A. M.; Frolov, S. M.; Kouwenhoven, L. P. *Phys. Rev. Lett.* **2013**, *110* (6), 66806.
(17) Kloeffel, C.; Trif, M.; Loss, D. *Phys. Rev. B: Condens. Matter Mater. Phys.* **2011**, *84* (19), 195314.
(18) Chuang, P.; Ho, S.-C.; Smith, L. W.; Sfigakis, F.; Pepper, M.; Chen, C.-H.; Fan, J.-C.; Griffiths, J. P.; Farrer, I.; Beere, H. E.; Jones, G. A. C.; Ritchie, D. A.; Chen, T.-M. *Nat. Nanotechnol.* **2015**, *10* (1), 35−39.
(19) Debray, P.; Rahman, S. M. S.; Wan, J.; Newrock, R. S.; Cahay, M.; Ngo, A. T.; Ulloa, S. E.; Herbert, S. T.; Muhammad, M.; Johnson, M. *Nat. Nanotechnol.* **2009**, *4*, 759.
(20) Gooth, J.; Schaller, V.; Wirths, S.; Schmid, H.; Borg, M.; Bologna, N.; Karg, S.; Riel, H. *Appl. Phys. Lett.* **2017**, *110*, 083105.
(21) Liang, G.; Xiang, J.; Kharche, N.; Klimeck, G.; Lieber, C. M.; Lundstrom, M. *Nano Lett.* **2007**, *7* (3), 642.
(22) Pedder, C. J.; Meng, T.; Tiwari, R. P.; Schmidt, T. L. *Phys. Rev. B: Condens. Matter Mater. Phys.* **2016**, *94* (24), 245414.
(23) Khrapai, V. S.; Nagaev, K. E. Finite Difference Time Domain (FDTD) Simulations of Electromagnetic Wave Propagation Using a Spreadsheet. 2018, arXiv:1805.12385. arXiv.org e-Print archive. https://arxiv.org/abs/1805.12385 (accessed June 28, 2018).
(24) Estrada Saldaña, J. C.; Niquet, Y.-M.; Cleuziou, J.-P.; Lee, E. J. H.; Car, D.; Plissard, S. R.; Bakkers, E. P. A. M.; De Franceschi, S. *Nano Lett.* **2018**, *18* (4), 2282.
(25) Roddaro, S.; Fuhrer, A.; Brusheim, P.; Fasth, C.; Xu, H. Q.; Samuelson, L.; Xiang, J.; Lieber, C. M. *Phys. Rev. Lett.* **2008**, *101* (18), 186802.
(26) Hu, Y.; Churchill, H. O. H.; Reilly, D. J.; Xiang, J.; Lieber, C. M.; Marcus, C. M. *Nat. Nanotechnol.* **2007**, *2* (10), 622−625.
(27) Brauns, M.; Ridderbos, J.; Li, A.; Bakkers, E. P. A. M.; Zwanenburg, F. A. *Phys. Rev. B: Condens. Matter Mater. Phys.* **2016**, *93* (12), 121408.
(28) Maier, F.; Kloeffel, C.; Loss, D. *Phys. Rev. B: Condens. Matter Mater. Phys.* **2013**, *87* (16), 161305.
(29) Wang, R.; Deacon, R. S.; Yao, J.; Lieber, C. M.; Ishibashi, K. *Semicond. Sci. Technol.* **2017**, *32* (9), 094002.
(30) Manchon, A.; Koo, H. C.; Nitta, J.; Duine, R. A.; Frolov, S. M. *Nat. Mater.* **2015**, *14* (9), 871.
(31) Yao, J.; Yan, H.; Das, S.; Klemic, J. F.; Ellenbogen, J. C.; Lieber, C. M. *Proc. Natl. Acad. Sci. U. S. A.* **2014**, *111* (7), 2431−2435.
(32) Zomer, P. J.; Guimarães, M. H. D.; Brant, J. C.; Tombros, N.; van Wees, B. *Appl. Phys. Lett.* **2014**, *105* (1), 013101.
(33) Castellanos-Gomez, A.; Buscema, M.; Molenaar, R.; Singh, V.; Janssen, L.; van der Zant, H. S. J.; Steele, G. A. *2D Mater.* **2014**, *1* (1), 011002.
(34) Wang, R.; Deacon, R. S.; Car, D.; Bakkers, E. P. a. M.; Ishibashi, K. *Appl. Phys. Lett.* **2016**, *108* (20), 203502.

DOI: 10.1021/acs.nanolett.8b01799
Nano Lett. 2018, 18, 6144−6149